Electronic Supplementary Information for

Merging the chemistry of metal-organic and polyoxometalate clusters into an enhanced photocatalytic material

Jon Napal,[a] Beñat Artetxe,[a] Garikoitz Beobide,*[a,c] Oscar Castillo,*[a,c] Antonio Luque,[a,c] Jon Pascual-Colino,[a] Sonia Pérez-Yáñez,[b,c] and Maite Perfecto-Irigaray[a]

[a] *Department of Organic and Inorganic Chemistry, University of the Basque Country, UPV/EHU, P.O. 644, E-48080 Bilbao, Spain.*
[b] *Department of Organic and Inorganic Chemistry, University of the Basque Country, UPV/EHU, E-01006 Vitoria-Gasteiz, Spain.*
[c] *BCMaterials, Basque Center for Materials, Applications and Nanostructures, UPV/EHU Science Park, E-48940 Leioa, Spain.*

S1. SYNTHESIS

Chemicals. Zirconium(IV) chloride ($ZrCl_4$, Alfa Aesar, 99.5%), caesium chloride (CsCl, Sigma-Aldrich, 98%), $H_4SiW_{12}O_{40}{\cdot}xH_2O$ (Sigma-Aldrich, 98%,), benzoic acid ($C_7H_6O_2$, Sigma-Aldrich, 99.5%), hydrochloric acid (HCl, Lab-Kem, 35-38%), benzene-1,4-dicarboxylic acid ($C_8H_6O_4$, Sigma-Aldrich, 98%), ethanol (C_2H_6O, Scharlau, 96%), propan-1-ol (C_3H_8O, Panreac, 99.5%), dimethylformamide (C_3H_7NO, Lab-Kem, 99.9%) and methylene blue ($C_{16}H_{18}ClN_3S$, Sigma-Aldrich, 99%) were used as commercially obtained.

Synthesis of $[Zr_6(\mu_3\text{-}O)_4(\mu_3\text{-}OH)_4(\mu\text{-}OOCC_6H_5)_8(H_2O)_8][SiW_{12}O_{40}]{\cdot}13EtOH$ (Zr_6/W_{12}-MC) and $[Zr_6(\mu_3\text{-}O)_4(\mu_3\text{-}OH)_4(\mu\text{-}OOCC_6H_5)_8(H_2O)_8][SiW_{12}O_{40}]{\cdot}11EtOH$ (Zr_6/W_{12}-NP). $ZrCl_4$ (1.66 mmol, 0.389 g) was dissolved in 4.8 mL of ethanol and subsequently 11.10 mmol of H_2O (200 µL) and 3.32 mmol of benzoic acid (0.407 g) dissolved in 8 mL of ethanol were added. The mixture was stirred for 5 minutes and thereafter, 0.27 mmol of the powdered solid $H_4SiW_{12}O_{40}{\cdot}xH_2O$ (0.793 g) were added. The pH of the reaction mixture[1] was shifted from -0.5 to 0.2 by adding 2 mL of water. The resulting solution was left to stand at room temperature. Few days later, **Zr_6/W_{12}-MC** crystallized as colourless rectangular plate-shaped crystals. Otherwise, setting the pH of the reaction to 0.8, the precipitation of a fine white powder corresponding to **Zr_6/W_{12}-NP** took place. Both **Zr_6/W_{12}-MC** and **Zr_6/W_{12}-NP** were filtered off, washed with ethanol and dried under vacuum. Elemental analysis for **Zr_6/W_{12}-MC**: Exp. (%): C: 18.23, H: 2.88, W: 43.09, Zr: 10.05; Cald. (%): C: 18.75, H: 2.40, W: 42.00, Zr: 10.42. Elemental analysis for Zr_6/W_{12}-NP: Exp. (%): C: 18.88, H: 2.78, W: 42.27, Zr: 11.05; Calc. (%): C: 18.15, H: 2.25, W: 42.74, Zr: 10.60.

Synthesis of $Cs_{3.5}H_{0.5}[SiW_{12}O_{40}]{\cdot}24H_2O$ (Cs/W_{12}). **Cs/W_{12}** was prepared following a previously reported procedure.[2] An aqueous solution (5 mL) of CsCl (1.07 mmol, 0.183 g) was added dropwise onto 0.27 mmol of $H_4SiW_{12}O_{40}$ (0.793 g) dissolved in 10 mL of water. Immediately after, **Cs/W_{12}** precipitated as a white polycrystalline powder. The compound was filtered off, washed with water and dried under vacuum.

Synthesis of $[Zr_6(\mu_3\text{-}O)_4(\mu_3\text{-}OH)_4(\mu_4\text{-}C_6H_4(COO)_2)_6]_n$ (UiO-66). **UiO-66** was prepared following a previously reported procedure.[3] $ZrCl_4$ (0.106 g, 0.454 mmol) and benzene-1,4-dicarboxylic acid (H_2BDC) (0.680 g, 0.454 mmol) were mixed in dimethylformamide (DMF) and heated in a sealed flask at 120 °C during 24 h. The obtained product was filtered off and thoroughly washed with DMF and ethanol.

[1] If the calibration of the electrode is performed in aqueous buffers, but the measurement is performed in a different solvent, the measured pH requires to subtract a correction constant: ${}^s_spH = {}^s_wpH - \delta$, where ${}^s_spH$ and ${}^s_wpH$ would in this case correspond to the pH for solvent media and measured pH, while δ is a correction constant. This constant depends of the solvent and it can be approached to –2.54 for ethanol. The pH values mentioned in the synthesis have not been corrected and correspond to ${}^s_wpH$. Note that the term ${}^w_wpH$ is used for the pH of an aqueous solution when the glass electrode has been calibrated with aqueous buffers. The mixed term ${}^s_wpH$ is used when the calibration is performed in aqueous buffers but the measurement is performed in a different solvent. Similarly, ${}^s_spH$ is used if the correction constant has been subtracted from the measured ${}^s_wpH$. See details in: G. T. T. Gibson, M. F. Mohamed, A. A. Neverov, R. S. Brow, *Inorg. Chem.*, 2006, **45**, 7891-7902; R. G. Bates, M. Paabo, R. A. Robinson, *J. Phys. Chem.*, 1963, **67**, 9, 1833–1838.

[2] Y. Kamiya, S. Sano, Y. Miura, Y. Uchida, Y. Ogawa, Y. Iwase and T. Okuhara, *Chem. Lett.*, 2010, **39**, 881–883.

[3] J. H. Cavka, S. Jakobsen, U. Olsbye, N. Guillou, C. Lamberti, S. Bordiga and K. P. Lillerud, *J. Am. Chem. Soc.*, 2008, **130**, 13850–13851.

S2. PHYSICAL MEASUREMENTS

Dinitrogen adsorption data were recorded at 77 K with a Quantachrome Autosorb-iQ MP. Prior to measurements all samples were outgassed under vacuum at 120 °C for 6 hours. The surface area values were obtained by the fittings of the N_2 adsorption data to Brunauer-Emmett-Teller (BET) equation.[4] In order to choose the appropriate pressure range and to avoid ambiguity when reporting the BET surface area of microporous materials the criteria recommended by the IUPAC was employed.[5]

Elemental analysis of C and H was performed on a EuroVector elemental analyzer, whereas metal contents were determined by inductively coupled plasma atomic emission spectrometer (ICP-AES; Horiba Yobin Yvon Activa).

Fourier-transform infrared (FTIR) spectra of the samples (KBr pellet) were recorded at a resolution of 4 cm^{-1} in the 4000–500 cm^{-1} region using a FTIR 8400S Shimadzu spectrometer.

Powder X-ray diffraction (PXRD) measurements were performed on a Phillips X'PERT diffractometer (equipped with Cu-Kα radiation, λ = 1.5418 Å) over the 5-70° 2θ range with a step size of 0.02°, a variable automatic divergence slit and an acquisition time of 2.5 s per step, at 20 °C.

Proton nuclear magnetic resonance (^{1}H-NMR) spectra were acquired in a Bruker AVANCE 5OO (one-bay; 500 MHz) at 293 K. Solvent residual signals arising from the proton of isotopomers of the solvent (deuterium oxide, 4.79 ppm) was used as reference for the signal positions.

Thermal analysis (TGA) was performed on a METTLER TOLEDO TGA/SDTA851 thermal analyzer in synthetic air (80% N_2, 20% O_2) flux of 50 $cm^3 \cdot min^{-1}$, from room temperature to 800 °C with heating rate of 5 °C min^{-1} and a sample size of about 10–20 mg per run.

Transmission electron microscopy (TEM) studies were done on a TECNAI G2 20 TWIN operated at 200 kV and equipped with LaB_6 filament, X-ray microanalysis unit (EDX) and STEM unit with light field/dark field detector. The samples for TEM were prepared by dispersion into ethanol solvent and keeping the suspension in an ultrasonic bath for 15 min, later a drop of suspension was spread onto a TEM copper grid (300 Mesh) covered by a holey carbon film followed by drying under vacuum.

Variable-temperature PXRD data were collected on a Bruker D8 Advance diffractometer operating at 30 kV and 20 mA, equipped with a Cu tube (λ = 1.5418 Å), a Vantec-1 PSD detector, and an Anton Parr HTK2000 high-temperature furnace. The powder patterns were recorded in the 5–38° 2θ range using steps of 0.033° and 1 s per step. Data sets were recorded in air atmosphere each 20 °C from 30 to 810 °C, using a heating rate of 0.17 °C·s^{-1}.

[4] S. Brunauer, P. H. Emmet and E. J. Teller, *J. Am. Chem. Soc.*, 1938, **60**, 309–319
[5] M. Thommes, K. Kaneko, A. V. Neimark, J. P. Oliver, F. Rodriguez-Reinoso, J. Rouquerol and K. S. W. Sing, *Pure Appl. Chem.*, 2015, **87**, 1051.

S3. SINGLE CRYSTAL X-RAY DIFFRACTION

Single-crystal X-ray diffraction data were collected at 150 K on an Agilent Technologies Supernova diffractometer with graphite monochromator and Mo−K_α radiation (λ = 0.71073 Å). Data reduction was done with the CrysAlisPro program[6] The details of the structure determination and refinement of **Zr_6/W_{12}-MC** are gathered in Table S1. The crystal structure was solved by direct methods using the SIR92 program[7] and refined by full-matrix least-squares on F^2 including all reflections (SHELXL97).[8] All calculations for these structures were performed using the WINGX crystallographic software package.[9]

All non-hydrogen atoms of the Zr_6 anionic entity were refined with anisotropic displacement parameters. The two crystallographically independent W_{12} are disordered. However in the first W_{12} entity the disorder involves the Si1 atom is distributed between two positions relatively close (0.33 Å) and it propagates along the entire anionic entity. In the second W_{12} entity the disorder is driven by a centre of inversion sited on the central Si2 atom and it only affects the oxygen atoms bonded to it. It means all the atoms of the first W_{12} entity were kept isotropic. Once the initial structure solution was completed, the difference Fourier map showed the presence of substantial electron density at the voids of the crystal structure that was impossible to model. Therefore, its contribution was subtracted from the reflection data by the SQUEEZE routine[10] as implemented in PLATON.[11] The structural disorder found in the POM anion and the large amount of heavy atoms (W) in the unit cell explains the presence of relatively high residual electron density peaks in the final structural resolution.

Table S1 Crystallographic data and structure refinement details of Zr_6/W_{12}-MC.

Empirical formula	$C_{78}H_{126}O_{83}SiW_{12}Zr_6$	**V (Å^3)**	6247.4(3)
Formula weight	5173.39	**T (K)**	150.0(1)
Crystal system	triclinic	**Z**	2
Space group	$P\bar{1}$	**ρ_{calcd} (g·cm^{-3})**	2.750
a (Å)	14.6248(4)	**μ (mm^{-1})**	11.588
b (Å)	15.4043(4)	**R_{int}**	0.0288
c (Å)	30.7774(8)	**Goodness of fit (S)**[a]	1.215
α (°)	89.831(2)	**R_1**[b]**/wR_2[all data]**[c,d]	0.0622/0.1053
β (°)	79.266(2)	**R_1**[b]**/wR_2[I > 2σ(I)]**[c,d]	0.0546/0.1026
γ (°)	66.903(2)		

[a] $S = [\Sigma w(F_0^2 - F_c^2)^2 / (N_{obs} - N_{param})]^{1/2}$ [b] $R = \Sigma ||F_0| - |F_c|| / \Sigma |F_c|$; [c] $Rw = [\Sigma w(F_0^2 - F_c^2)^2 / \Sigma w \cdot F_c^2]^{1/2}$; [d] $w = 1/[\sigma^2(F_0^2) + (a*P)^2 + bP]$ where $P = (F_0^2 + 2*F_c^2)/3$, a = 0, and b = 142.6315.

[6] CrysAlisPRO, Oxford Diffraction /Agilent Technologies UK Ltd, Yarnton, England.
[7] A. Altomare, G. Cascarano, C. Giacovazzo, A. Guagliardi, M. C. Burla, G. Polidori and M. Camalli, *J. Appl. Cryst.*, 1994, **27**, 435.
[8] G. M. Sheldrick, *Acta Cryst.*, 2015, **C71**, 3–8.
[9] L. J. Farrugia, *J. Appl. Cryst.*, 2012, **45**, 849–854.
[10] P. Van der Sluis and A. L. Spek, *Acta Crystallogr. A*, 1990, **A46**, 194–201.
[11] A. L. Spek, *Acta Cryst.*, 2009, **D65**, 148-155.

S4. CRYSTAL STRUCTURE DATA

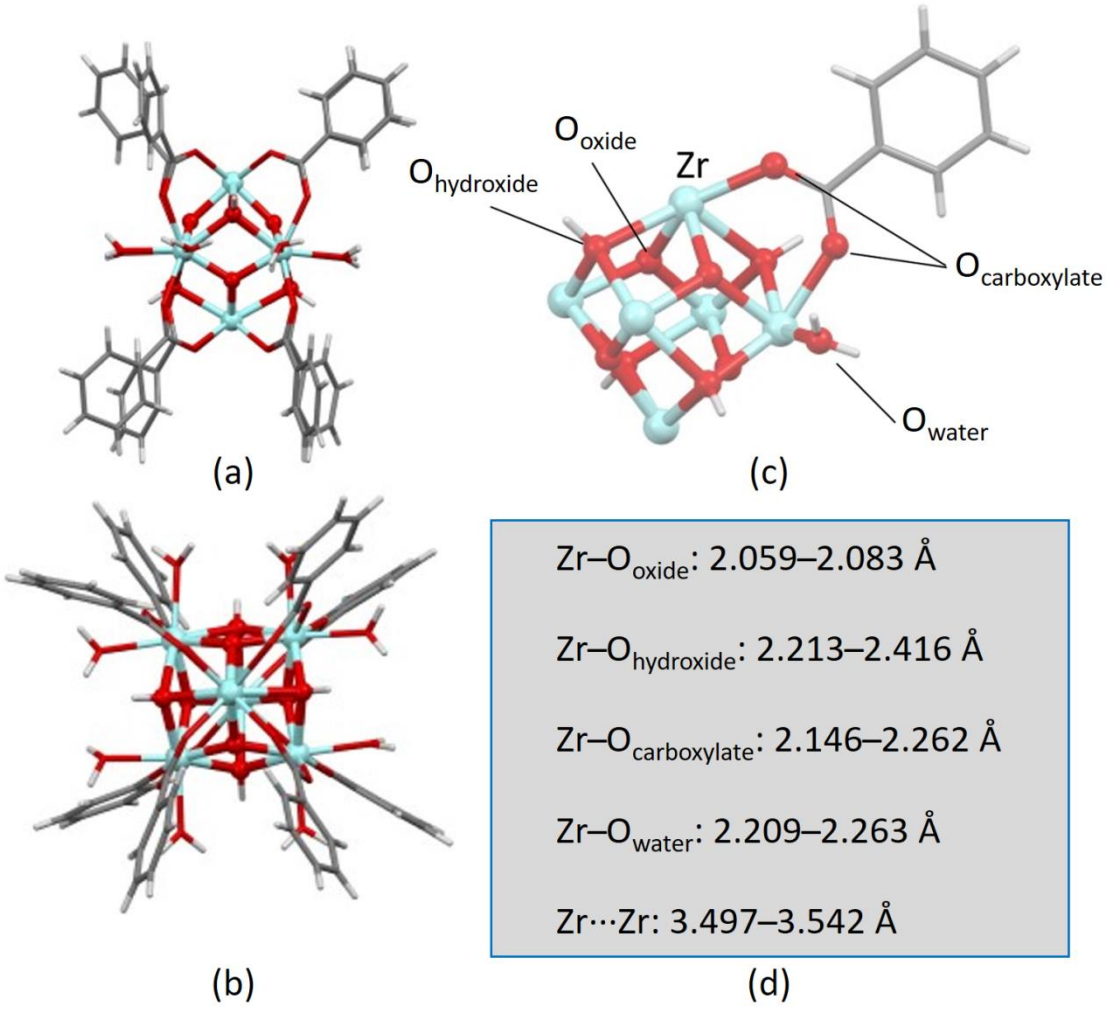

Fig. S1 (a) Side and (b) upper view of $[Zr_6(\mu_3\text{-}O)_4(\mu_3\text{-}OH)_4(\mu\text{-}OOCC_6H_5)_8(H_2O)_8]^{4+}$ entity in **Zr_6/W_{12}-MC**, together with (c) atom labelling scheme and (d) representative inter atomic distances.

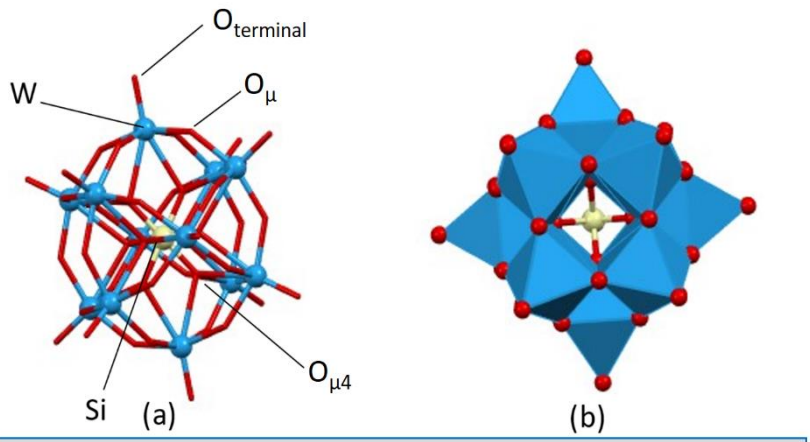

Si–O: 1.619–1.635 Å	W–$O_{\mu4}$: 2.209–2.263 Å
W–$O_{terminal}$: 1.659–1.685 Å	W···Si: 3.509–3.547 Å
W–O_{μ}: 1.877–1.927 Å	W···W: 3.552–3.526 Å

(c)

Fig. S2 (a) View of $[SiW_{12}O_{40}]^{4-}$ entity in **Zr_6/W_{12}-MC** showing the atom labelling scheme, together with (b) its polyhedral representation and (c) the most representative inter atomic distances.

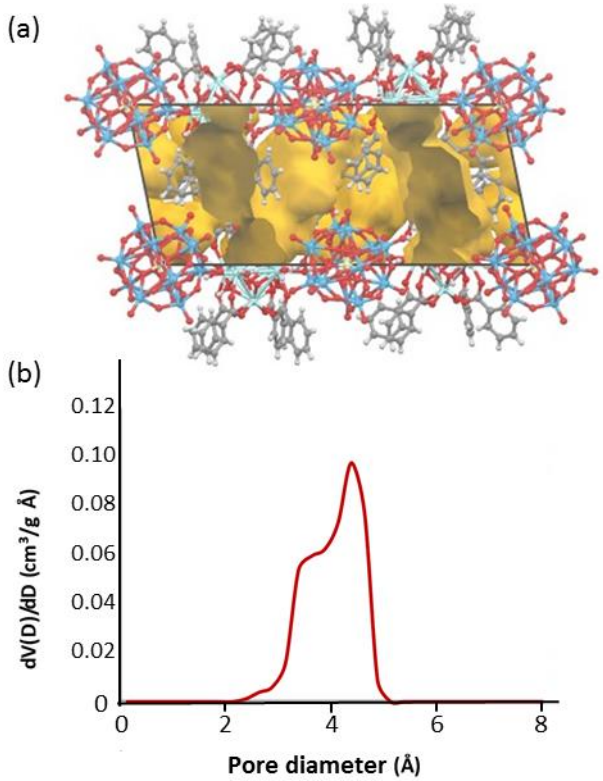

Fig. S3 (a) Crystal packing of **Zr_6/W_{12}-MC** viewed along the *b*-axis including the plot of the pore surface and (b) pore size distribution, revealing wide cavities of 4.4 Å connected by narrower necks of 3.6 Å.

S5. Powder X-Ray Diffraction Patterns

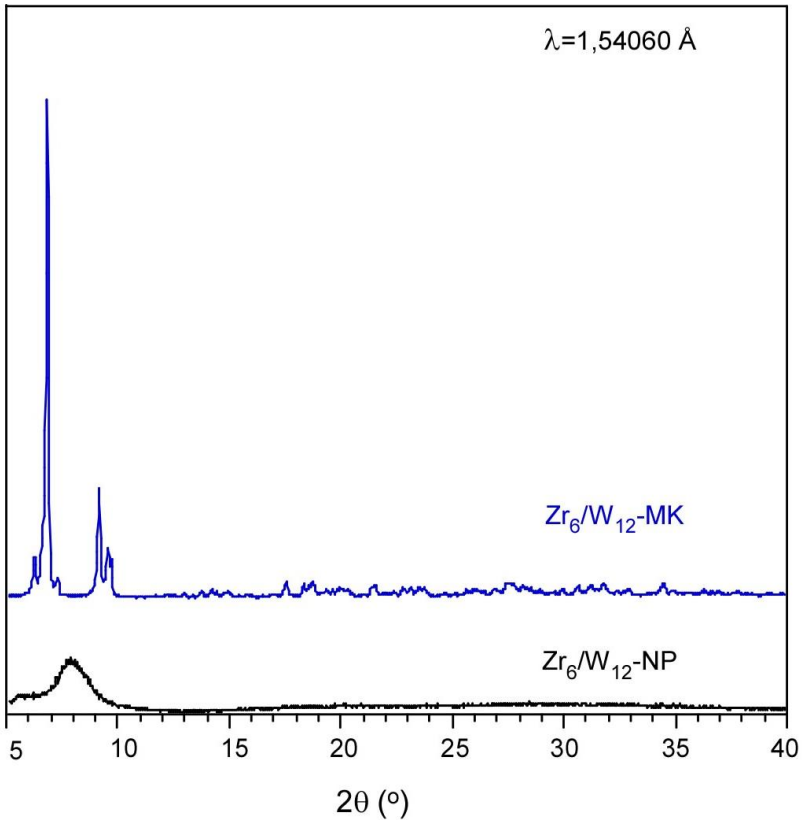

Fig. S4 Comparison of the PXRD patterns of **Zr_6/W_{12}-MC** (blue) and **Zr_6/W_{12}-NP** (black) highlighting their crystalline and amorphous nature,respectively.

S6. FOURIER TRANSFORM INFRARED SPECTRA

The FTIR spectra of **Zr_6/W_{12}-MC** and **Zr_6/W_{12}-NP** (Fig. S5) show a great resemblance as it can be expected for polymorphic compounds. Both show the main peaks of vibration modes corresponding to the molecular building blocks that comprise the compounds: $[Zr_6O_4(OH)_4(OOCC_6H_5)_8(H_2O)_8]^{4+}$ and $[SiW_{12}O_{40}]^{4-}$. The assignation of the vibration modes is gathered in Table S2.

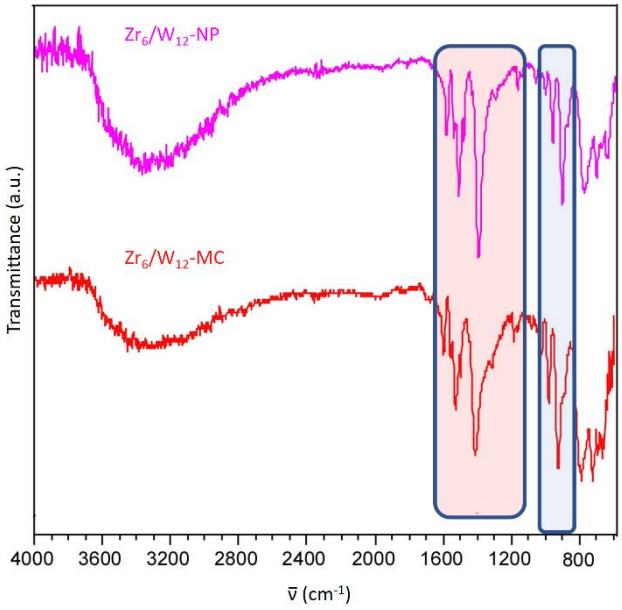

Fig. S5 FTIR spectra of **Zr_6/W_{12}-MC** and **Zr_6/W_{12}-NP**, highlighting the main signal of the metal-organic Zr-cluster (light pink) and of the polyoxotungstate (light blue).

Table S2 Main FTIR signals and assignation of the vibration modes for Zr_6/W_{12}-MC and Zr_6/W_{12}-NP.

Vibration mode	Zr_6/W_{12}-MC (cm^{-1})	Zr_6W_{12}-NP (cm^{-1})
ν(OH)	3700-2800 s	3700-2800 s
ν_{as}(C-O)	1600 m	1600 m
ν(C=C)$_{arom}$	1550 m	1550 m
ν_s(C-O)	1400 s	1400 m
δ_{pb}(C-H)$_{arom}$	1100 w,1020 w	1100 w,1020 w
ν(Si-O)	1120 vw	1120 vw
ν(W=O$_{terminal}$)	940 m	940 m
ν(W-O$_{-\mu}$)	900 s	900 s
δ_{op}(C-H)$_{arom}$	725 m	725 m
δ(COO^-)	688 sh	688 sh
ν(Zr-O^{2-})	657 m	657 m

[a]: s: = strong, m = medium, w = weak, vw = very weak, sh = shoulder.

S7. THERMAL ANALYSIS

Fig. S6 shows the thermogravimetric curves for Zr_6/W_{12}-MC and Zr_6/W_{12}-NP, while Tables S3 and S4 display the assignation of the mass losses. Note that the assignation of the mass losses fits to the expected formulas. Both compounds exhibit an initial mass loss from room temperature to *ca*. 160-170 °C corresponding to the evaporation of the solvent molecules hosted in the pores. Subsequently, the coordination water molecules of the Zr_6-cluster are released (> 160-170 °C). Close to 400 °C, the compounds are degraded in two consecutive mass losses, to render at 800 °C a residue comprised by a mixture of oxides which were identified by PXRD as WO_3 (ICDD: 00-032-1395), ZrO_2 (ICDD: 00-049-1746) and SiO_2 (ICDD: 01-076-0939; cristobalite).

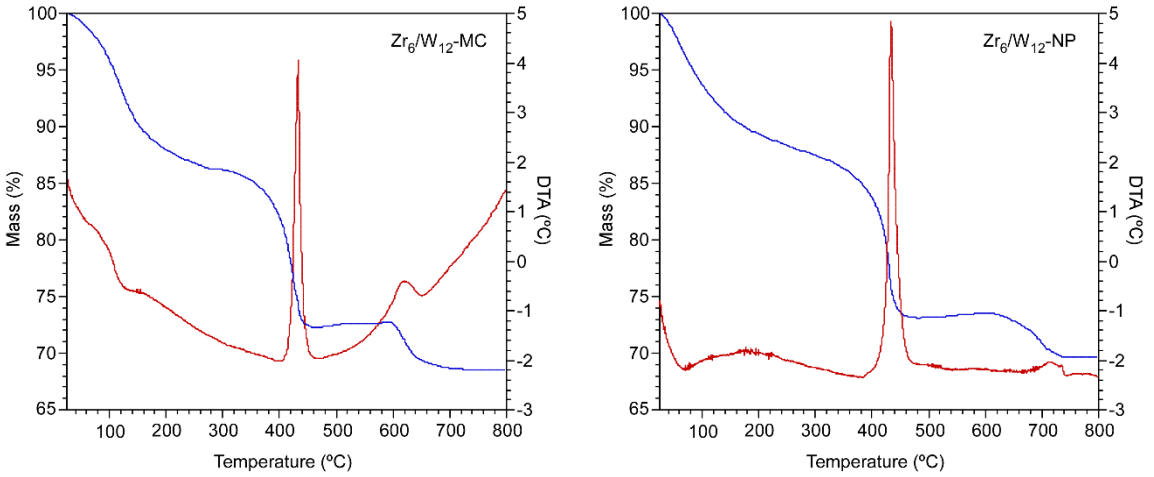

(a) (b)

Fig. S6 Plots of the thermogravimetric analysis (TGA) for (a) **Zr_6/W_{12}-MC** and (b) **Zr_6/W_{12}-NP** (mass change: blue line; differential thermal analysis (DTA): red line).

Table S3 Assignation of mass loss processes for the TGA data of Zr_6/W_{12}-MC.

T (°C)	Δm (%)	m_{exp} (%)	m_{theor} (%)	Product
25	---	100.00	99.86	$[Zr_6O_4(OH)_4(OOCC_6H_5OH)_8(H_2O)_8][SiW_{12}O_{40}]\cdot 13\ EtOH$
25-170 (endo)	11.38	88.62	88.50	$[Zr_6O_4(OH)_4(OOCC_6H_5OH)_8(H_2O)_8][SiW_{12}O_{40}]$
170-290 (endo)	2.62	86.00	85.76	$[Zr_6O_4(OH)_4(OOCC_6H_5OH)_8][SiW_{12}O_{40}]$
290-460 (exo)	14.69	71.31	71.24	$[Zr_6(CO_3)_4(O)_6][SiW_{12}O_{40}]$
600-690 (exo)	2.79	68.52	68.51	$[Zr_6O_{12}][SiW_{12}O_{38}]$

Table S4 Assignation of mass loss processes for the TGA data of Zr_6/W_{12}-NP.

T (°C)	Δm (%)	m_{exp} (%)	m_{theor} (%)	Product
25	---	100.00	99.90	$[Zr_6O_4(OH)_4(OOCC_6H_5OH)_8(H_2O)_8][SiW_{12}O_{40}]\cdot 11EtOH$
25-160 (endo)	9.32	90.68	90.64	$[Zr_6O_4(OH)_4(OOCC_6H_5OH)_8(H_2O)_8][SiW_{12}O_{40}]$
160-315 (endo)	3.41	87.27	87.86	$[Zr_6O_4(OH)_4(OOCC_6H_5OH)_8][SiW_{12}O_{40}]$
315-500 (exo)	14.07	73.20	72.81	$[Zr_6(CO_3)_4(O)_6][SiW_{12}O_{40}]$
620-740 (exo)	3.55	69.65	69.83	$[Zr_6O_{12}][SiW_{12}O_{38}]$

Fig. S7 shows the temperature-variable PXRD patterns of **Zr_6/W_{12}-MC**. Thereof, it can be concluded that the compound retains its crystal structure up to 350 °C. Then the diffraction peaks decay as consequence of the exothermic decomposition of the structure. Above 600 °C the emergence of the reflections corresponding to simple metal oxides can be observed.

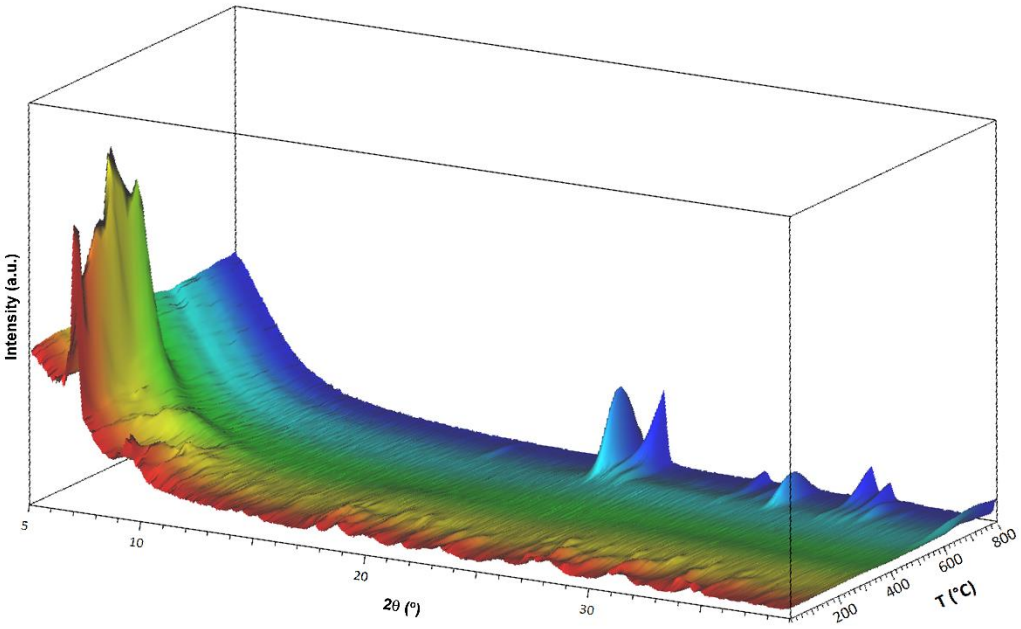

Fig. S7 Variable temperature PXRD patterns of **Zr_6/W_{12}-MC**.

S8. ADSORPTION ISOTHERMS

For comparative purposes the N_2 adsorption isotherms (77 K) for the herein reported compounds (**Zr_6/W_{12}-MC**, **Zr_6/W_{12}-NP**) and for the selected referential compounds (**Cs/W_{12}** and **UiO-66**) were measured (Fig. S8). Prior to the measurements, all the samples were outgassed under vacuum at 120 °C. **Zr_6/W_{12}-MC** and **Zr_6/W_{12}-NP** exhibit a negligible adsorption (S_{BET} = 1.5 and 1.2 m^2g^{-1}, respectively) which can be related to the hindered N_2 diffusion through the necks (3.6 Å) connecting the wider pores. Note that the kinetic radius of N_2 (3.64 Å) slightly exceeds the limiting pore size. In spite of the small crystallite size of **Zr_6/W_{12}-NP**, the lack of microstructural porosity is probably due to the strong aggregation occurring during the sample drying, as it happens in many colloidal systems. **Cs/W_{12}** exhibits a type I/IV adsorption isotherm with an elongated hysteresis loop, as a result of the combination of the intrinsic microporosity of the crystals and the microstructural mesoporosity rendered by the submicrometric particle size comprising the sample (see section S8). The total BET surface area for **Cs/W_{12}** is 152.6 m^2g^{-1} ($S_{micropore}$: 67.0 m^2g^{-1}; $S_{external}$: 85.6 m^2g^{-1}). The adsorption branch of **UiO-66** fits to a type I isotherm as expected for a microporous compound. The monotonic increase observed at intermediate pressures is caused again by the interparticle adsorption of the adsorbate. The total BET surface area for UiO-66 sample is 1351.8 m^2g^{-1} ($S_{micropore}$: 1289.4 m^2g^{-1}; $S_{external}$: 62.4 m^2g^{-1}).

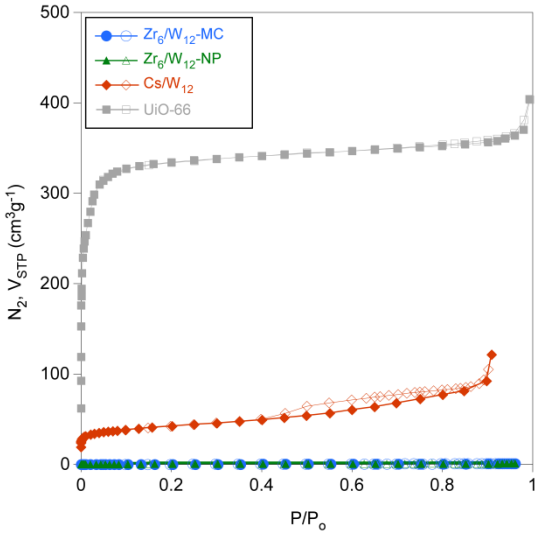

Fig. S8 N_2 adsorption isotherms at 77 K for **Zr_6/W_{12}-MC**, **Zr_6/W_{12}-NP**, **Cs/W_{12}** and **UiO-66** (adsorption branch: filled symbols; desorption branch: empty symbols).

In the case of **Zr_6/W_{12}-MC** the adsorption of molecules with smaller kinetic radius than N_2 were also tested: CO_2 (3.30 Å) at 273 K and H_2O (2.65 Å) at 293 K. The results, with maximum adsorption values of 0.30 mmol CO_2/g (when activated at 200°C) and 80 mg H_2O/g, indicate moderate but significant adsorption in agreement with the relatively low void percentage observed in the crystalline structure (28%) and the high density of **Zr_6/W_{12}**.

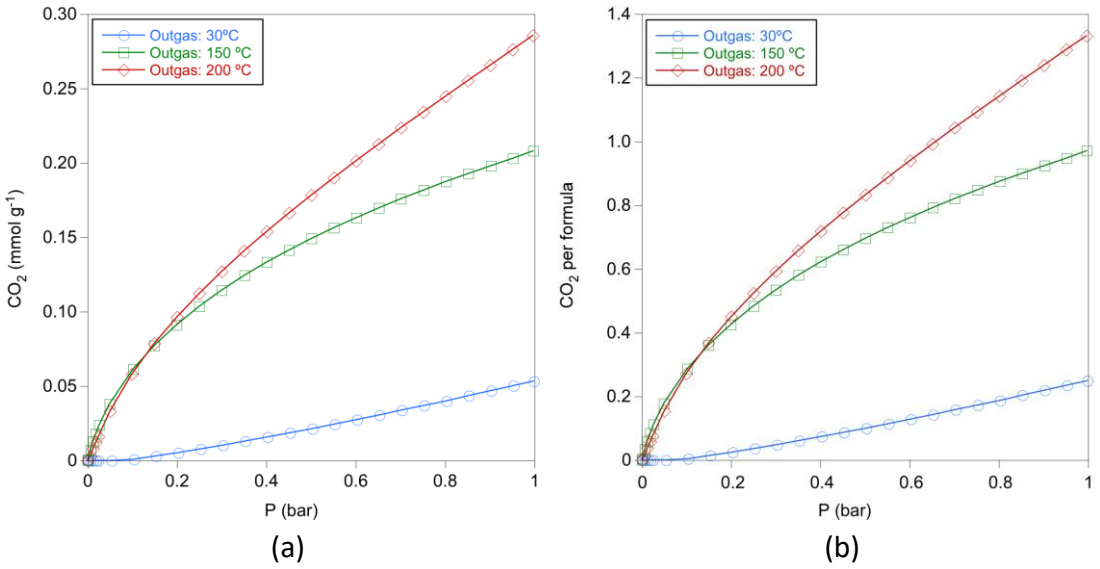

Fig. S9 CO_2 adsorption/desorption isotherm for **Zr_6/W_{12}-MC** at 273 K represented as (a) CO_2 mmol per sample weight and (b) CO_2 molecules per Zr_6W_{12} formula.

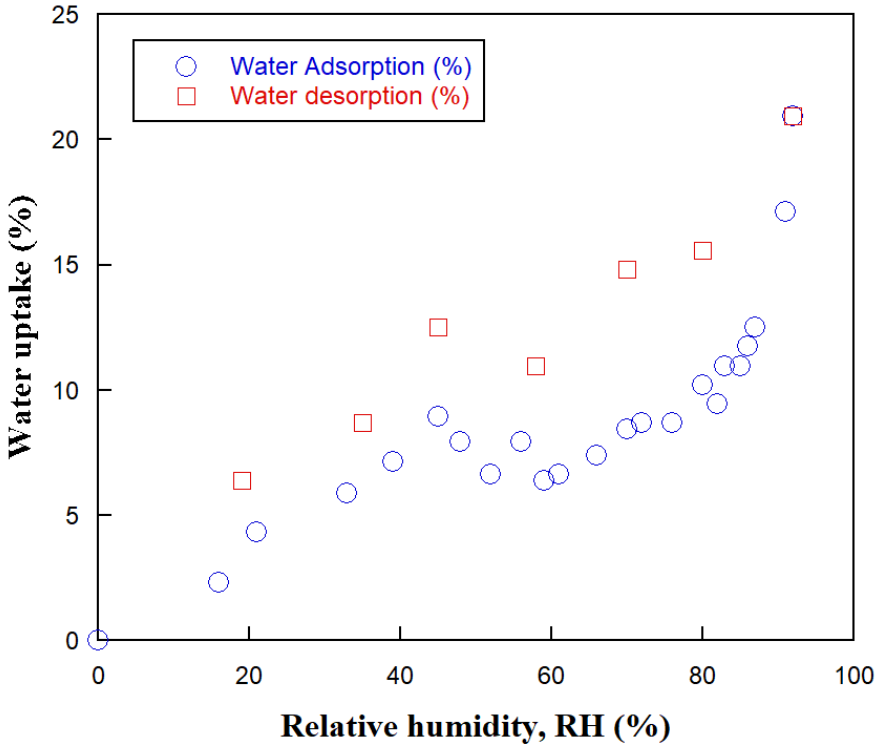

Fig. S10 Water vapour adsorption/desorption isotherm for **Zr_6/W_{12}-MC** at 293 K (blue circles adsorption and red squares desorption).

S9. ELECTRON MICROSCOPY IMAGES

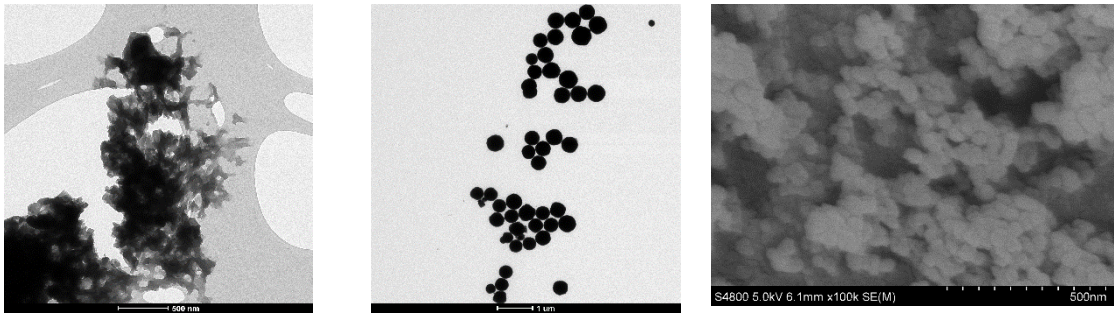

(a) (b) (c)

Fig. S11 Electron microscopy images: TEM images of (a) **Zr_6/W_{12}-NP** and (b) **Cs/W_{12}** and (c) SEM image of **UiO-66** sample.

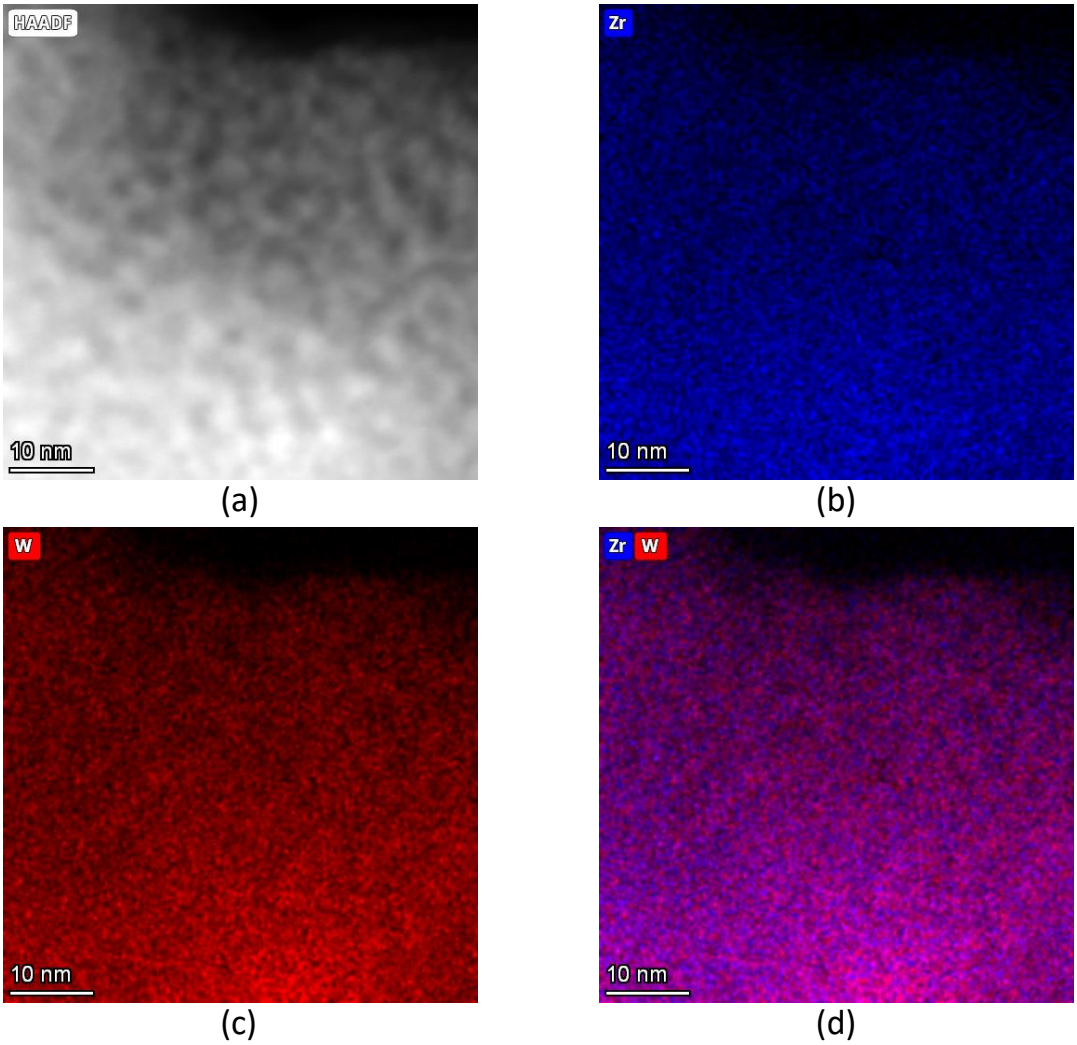

Fig. S12 TEM images taken on Zr_6W_{12}-NP showing the elemental distribution determined by EDXRF: (a) high-angle annular dark-field image and elemental distribution for (b) Zr, (c) W and (d) both Zr and W.

S10. CHEMICAL STABILITY

FTIR (**Zr_6/W_{12}-MC** and **Zr_6/W_{12}-NP**) and PXRD (**Zr_6/W_{12}-MC**) measurements were performed on samples submerged for 24 h in methanol, ethanol, water and 1 M HCl (aq) media.

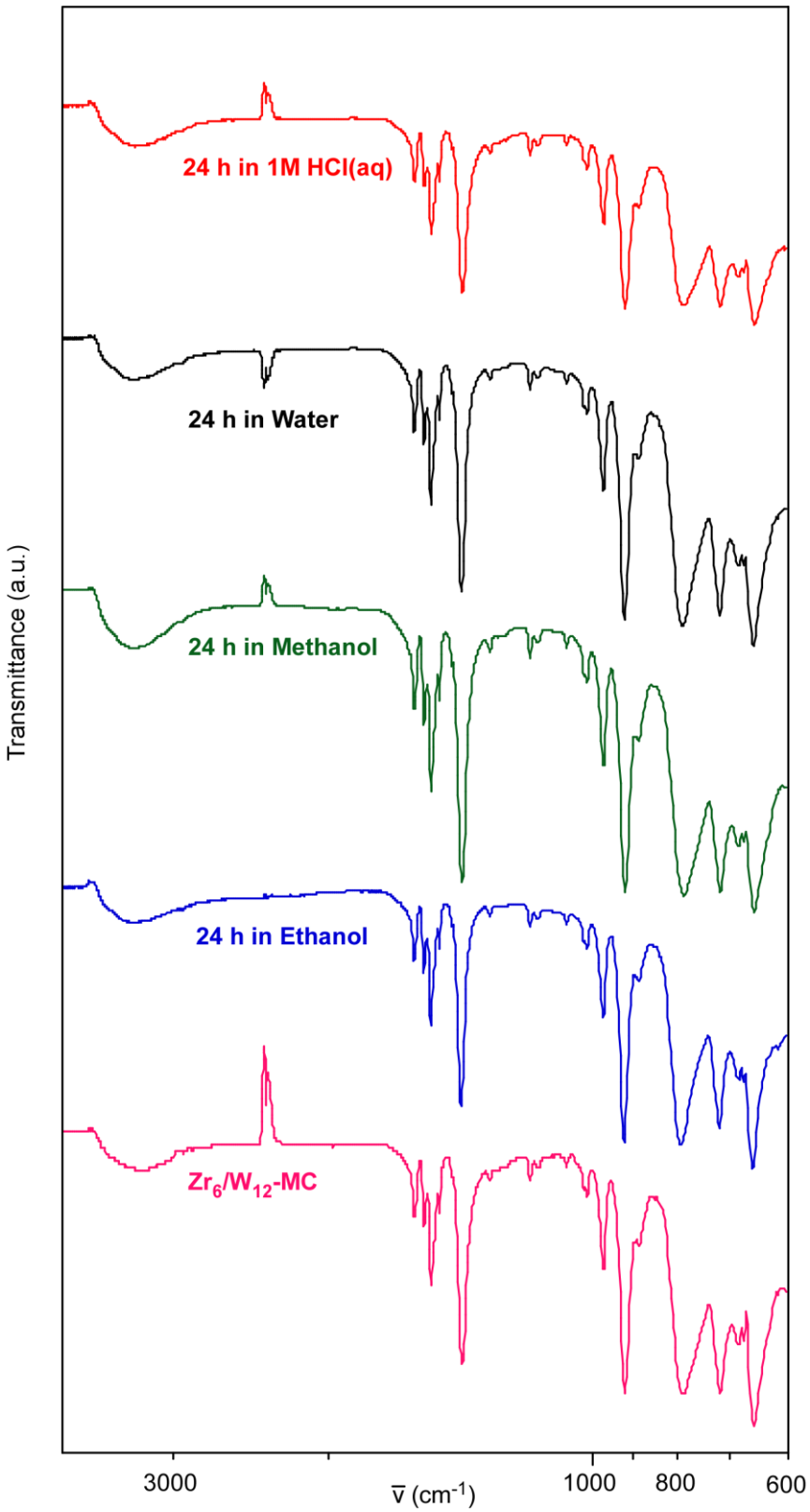

Fig. S13 FTIR spectra of pristine **Zr_6/W_{12}-MC** and the same sample after being submerged for 24 h in ethanol, methanol, water and 1 M HCl(aq) media.

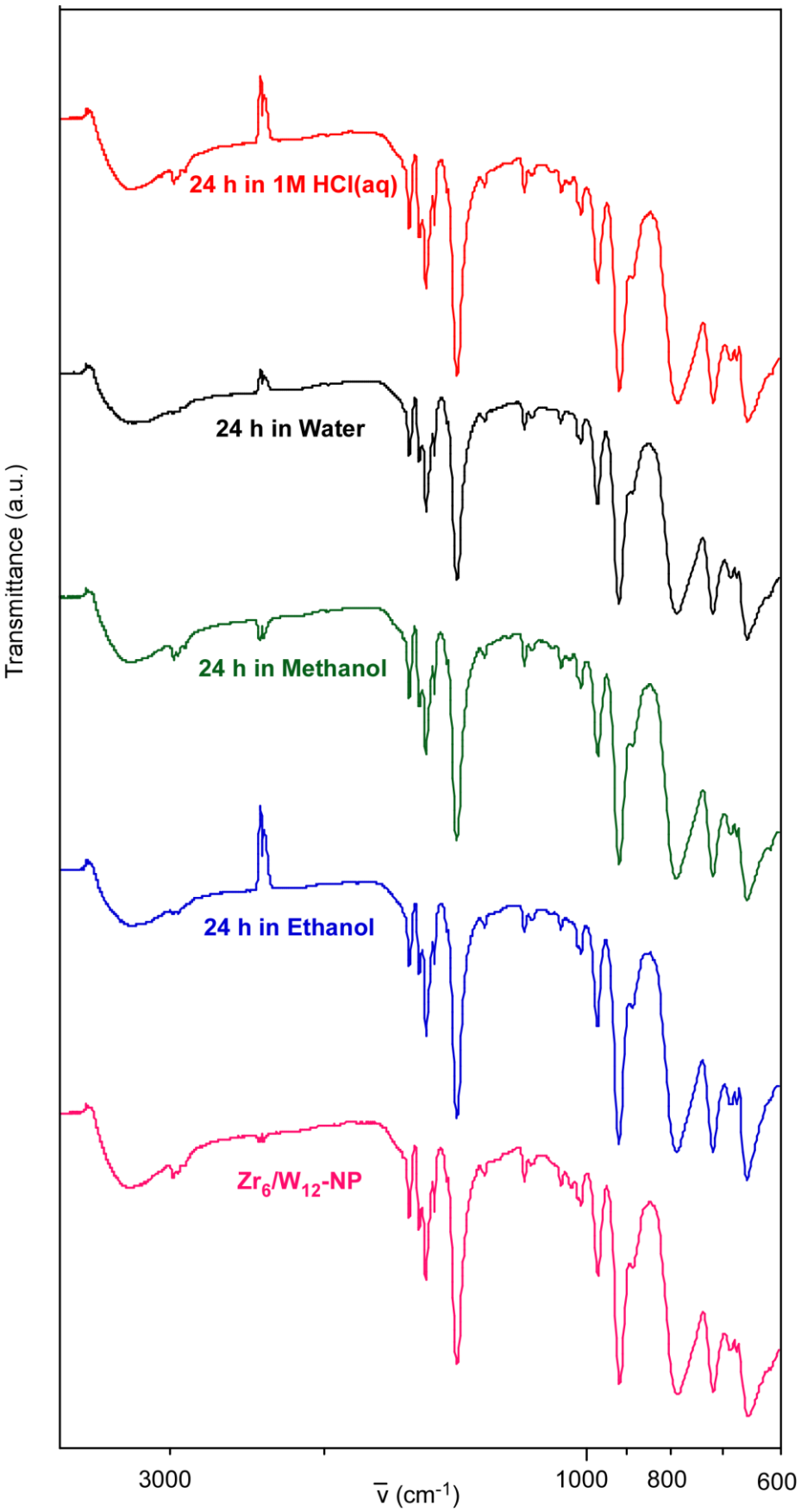

Fig. S14 FTIR spectra of pristine **Zr_6/W_{12}-NP** and the same sample after being submerged for 24 h in ethanol, methanol, water and 1 M HCl(aq) media.

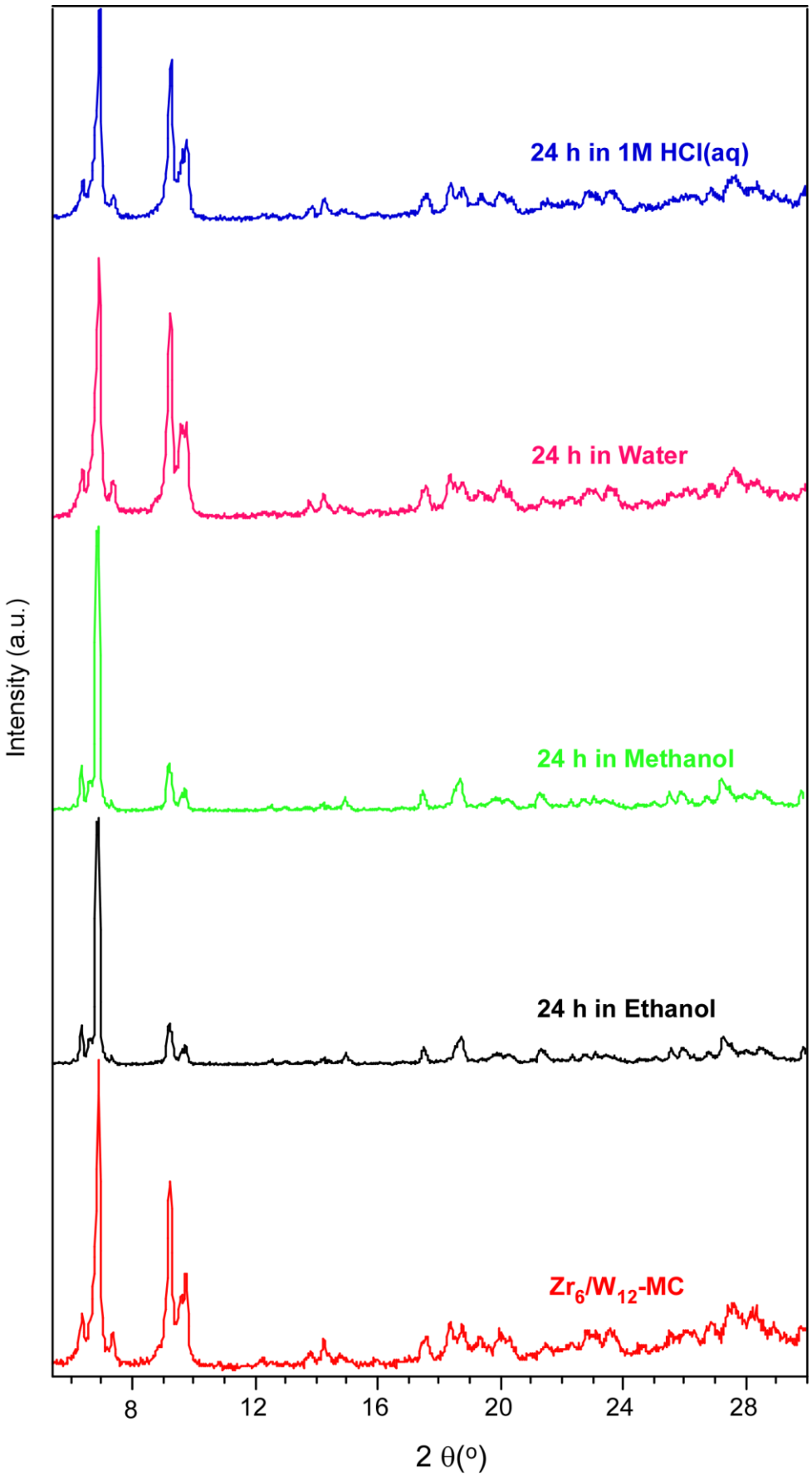

Fig. S15 PXRD pattern ($\lambda_{Cu\text{-}K\alpha}$: 1.5418 Å) of pristine **Zr_6/W_{12}-MC** and the same sample after being submerged for 24 h in ethanol, methanol, water and 1 M HCl(aq) media.

S11. PHOTOCATALYTIC EXPERIMENTS

METHYLENE BLUE PHOTODEGRADATION

Each photodegradation experiment was run using an aqueous solution (250 mL) of methylene blue (8 µM) at pH = 1 and 50 mg of the photocatalysts (**Zr_6/W_{12}-NP**, **Cs/W_{12}** or **UiO-66**). The pH of the reaction media was fixed using HCl (36%). A neodymium filament lamp (HEATING ND-20, 100 W) was selected as light source and sited vertically at 20 cm from the reaction flask. The reaction mixture was maintained under continuous stirring and the temperature was set to 20 °C using a cooled jacketed vessel. The reaction assembly (Fig. S16) was contained within a protective casing (photonCABINET from PESCHL Photoreactors) to isolate it from the external illumination and protect the user. The adsorption stage was performed in dark conditions, whereas the lamp was switched on to analyse the photochemical degradation. The evolution of the methylene blue concentration was assessed by monitoring its absorption maxima at 666 nm with a UV/VIS spectrophotomer (UV-1240, Shimadzu).

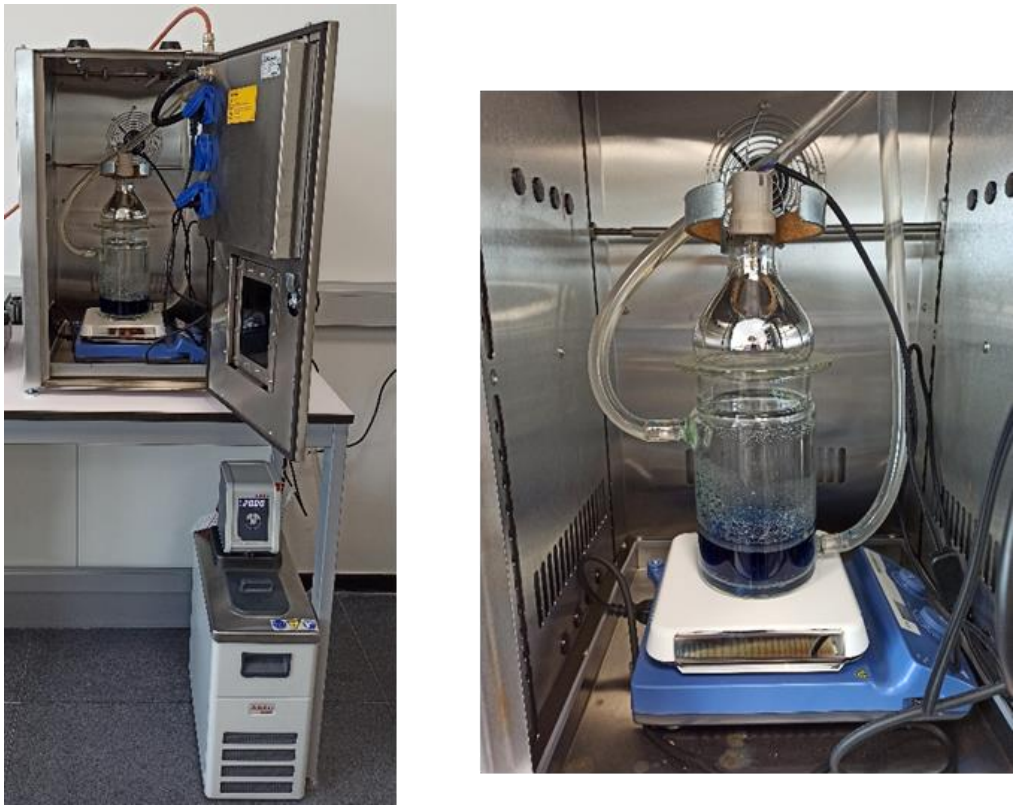

Fig. S16 Protective casing and cooling bath (left) and detail of the reaction assembly (right).

STABILITY OF THE CATALYST AFTER THE METHYLENE BLUE PHOTODEGRADATION EXPERIMENT

FTIR spectra (**Zr_6/W_{12}-MC** and **Zr_6/W_{12}-MC**) and PXRD (**Zr_6/W_{12}-MC**) of the catalyst previous and after the methylene blue photodegradation experiment were taken showing no significant changes.

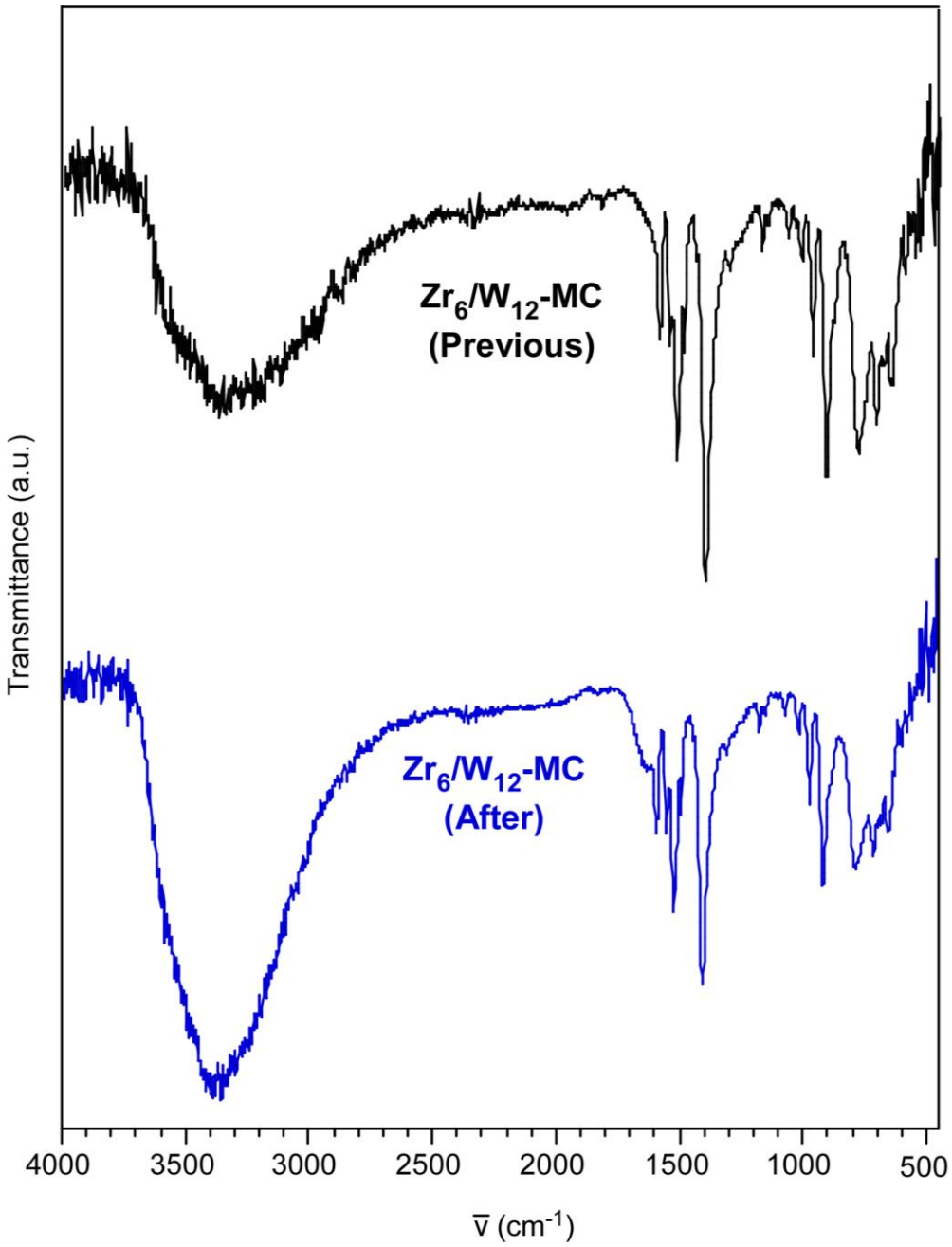

Fig. S17 FTIR spectra of pristine **Zr_6/W_{12}-MC** and the same sample after the methylene blue photodegradation experiment.

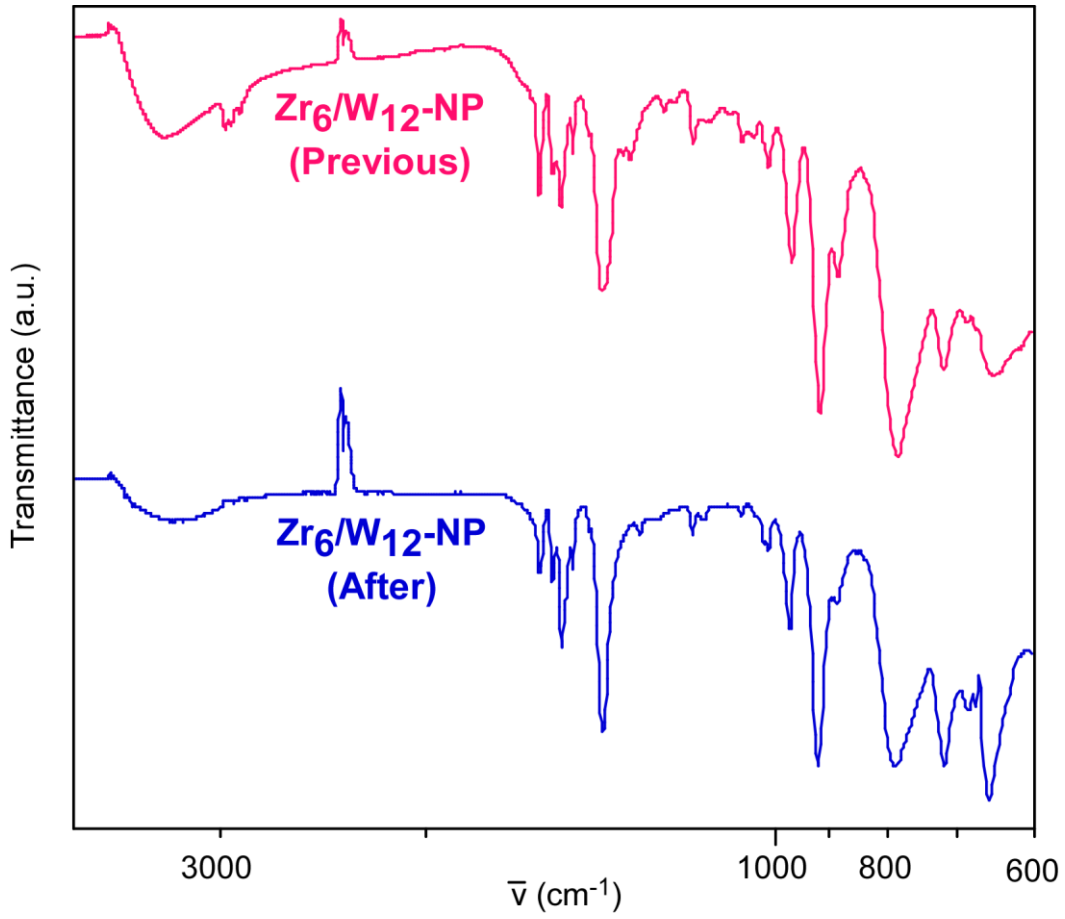

Fig. S18 FTIR spectra of pristine **Zr_6/W_{12}-NP** and the same sample after the methylene blue photodegradation experiment.

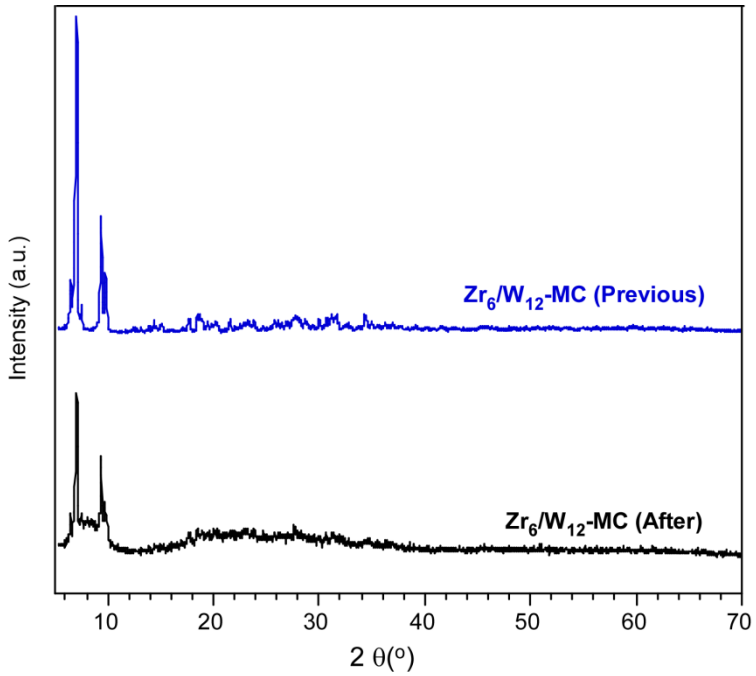

Fig. S19 PXRD pattern ($\lambda_{Cu\text{-}K\alpha}$: 1.5418 Å) of pristine **Zr_6/W_{12}-MC** and the same sample after the methylene blue photodegradation experiment.

BENZYL ALCOHOL PHOTO-OXIDATION

Each photodegradation experiment was run using a D_2O solution (2 mL) in which 20 µL of benzyl alcohol, 20 µL of HCl and 50 mg of the potentially photocatalytic material (**Zr_6/W_{12}**, **Cs/W_{12}**, **UiO-66** and **W_{12}@UiO-66**) were added. The mixture was placed in closed test tube with continuous stirring while under two conditions: a) upon exposure to the UV radiation coming from a Hg lamp (ORIEL 68810, 200-500 W) and b) in the dark without any exposure to visible or UV radiation (only adsorption). After four hours of continuous stirring 20 µL of *tert*-butanol were added to the mixture as internal standard and the solid catalyst was removed by filtration. A blank solution for the ^{1}H-NMR experiments was also prepared by mixing 2 mL of D_2O, 20 µL of benzyl alcohol, 20 µL of HCl and 20 µL of *tert*-butanol.

The ^{1}H-NMR spectra of these solutions were measured and the singlet signals at 1.20 and 4.59 ppm corresponding to the methyl groups of the *tert*-butanol and the CH_2 group of the benzyl alcohol, respectively, were integrated. The yielded values were employed to quantify the amount of benzyl alcohol remaining in the solution were obtained using as reference the values obtained for the blank solution (Figures S20-S23).

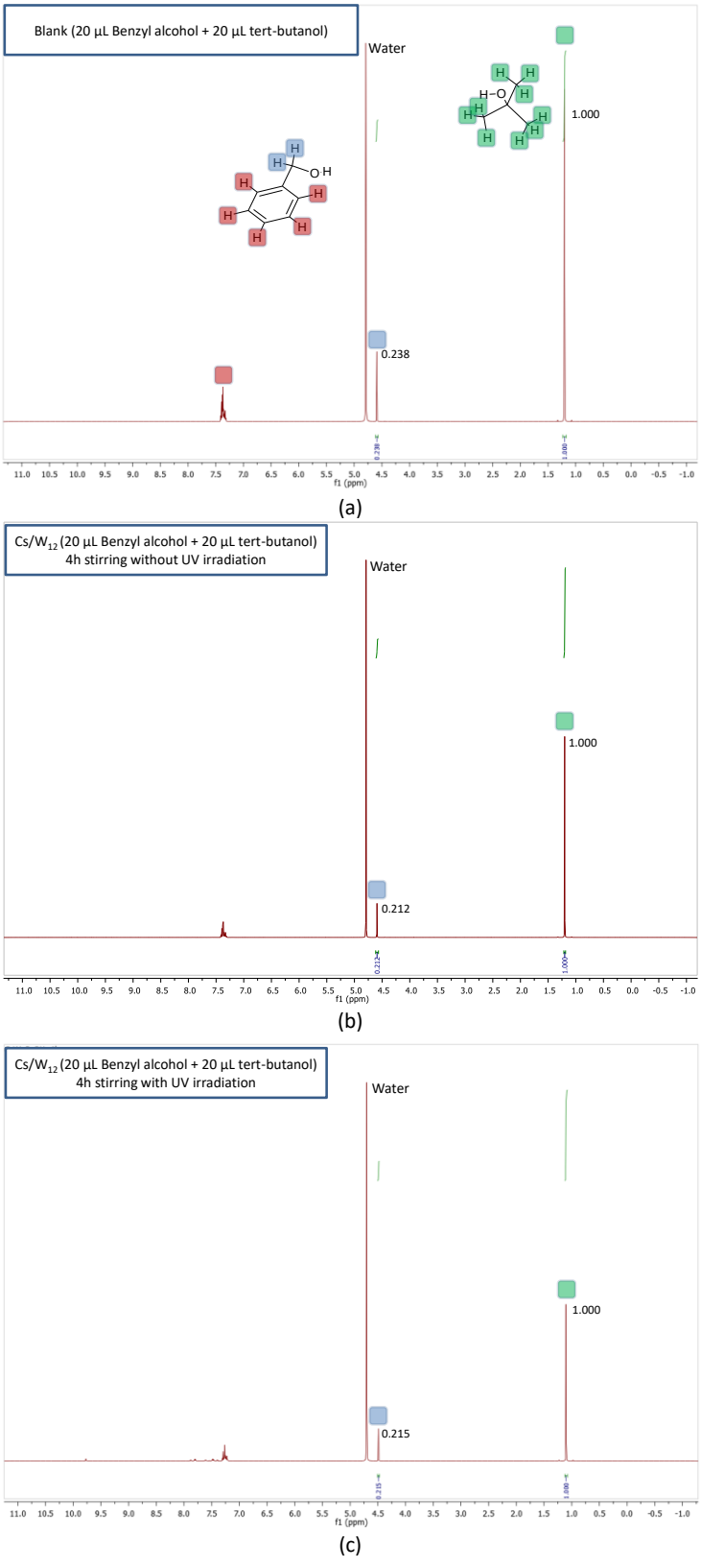

Fig. S20 (a) ^{1}H-NMR spectra of the blank solution, (b) the same blank solution after incorporating 50 mg of Cs/W_{12} and stirring for 4h, and (c) the same blank solution after incorporating 50 mg of Cs/W_{12} and stirring for 4h while irradiating with a Hg lamp.

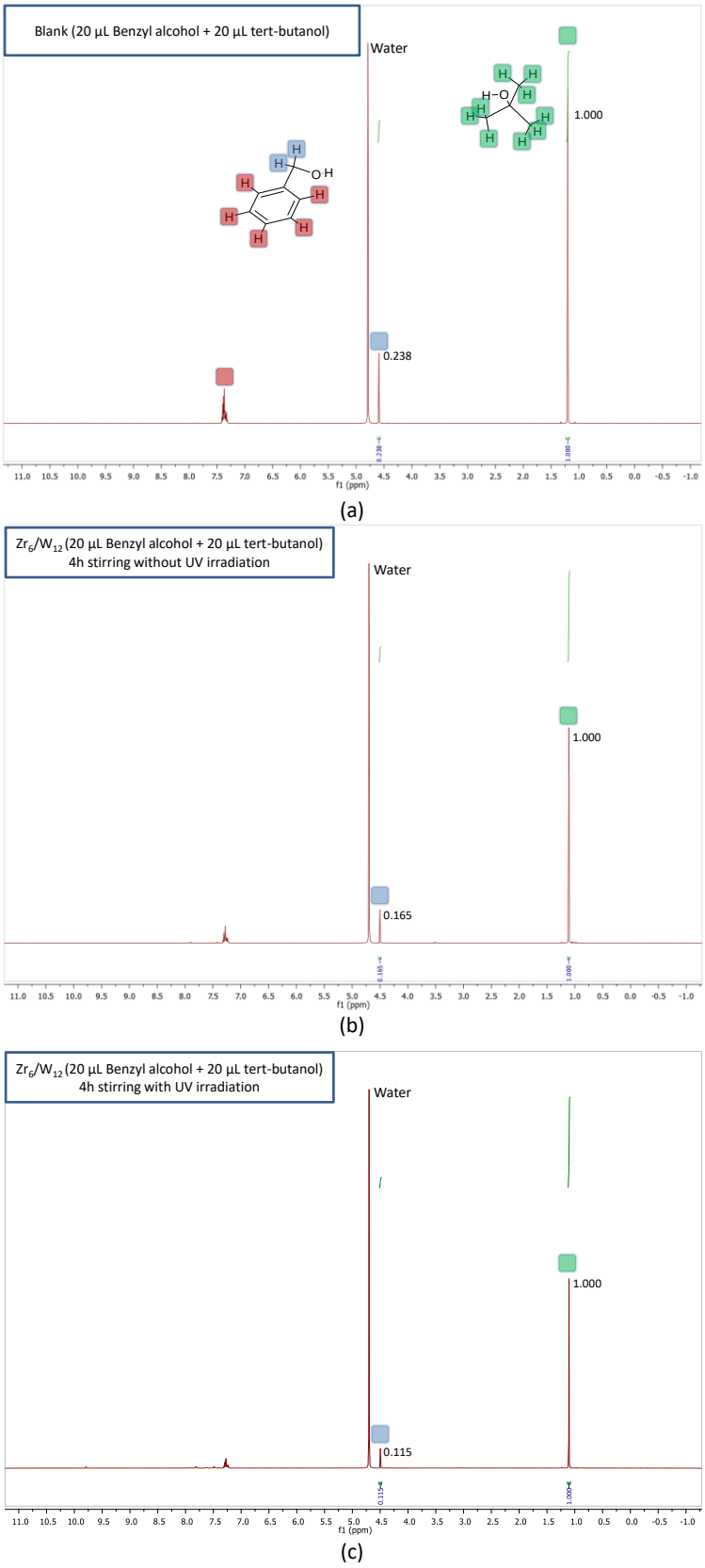

Fig. S21 (a) ^{1}H-NMR spectra of the blank solution, (b) the same blank solution after incorporating 50 mg of Zr_6/W_{12} and stirring for 4h, and (c) the same blank solution after incorporating 50 mg of Zr/W_{12} and stirring for 4h while irradiating with a Hg lamp.

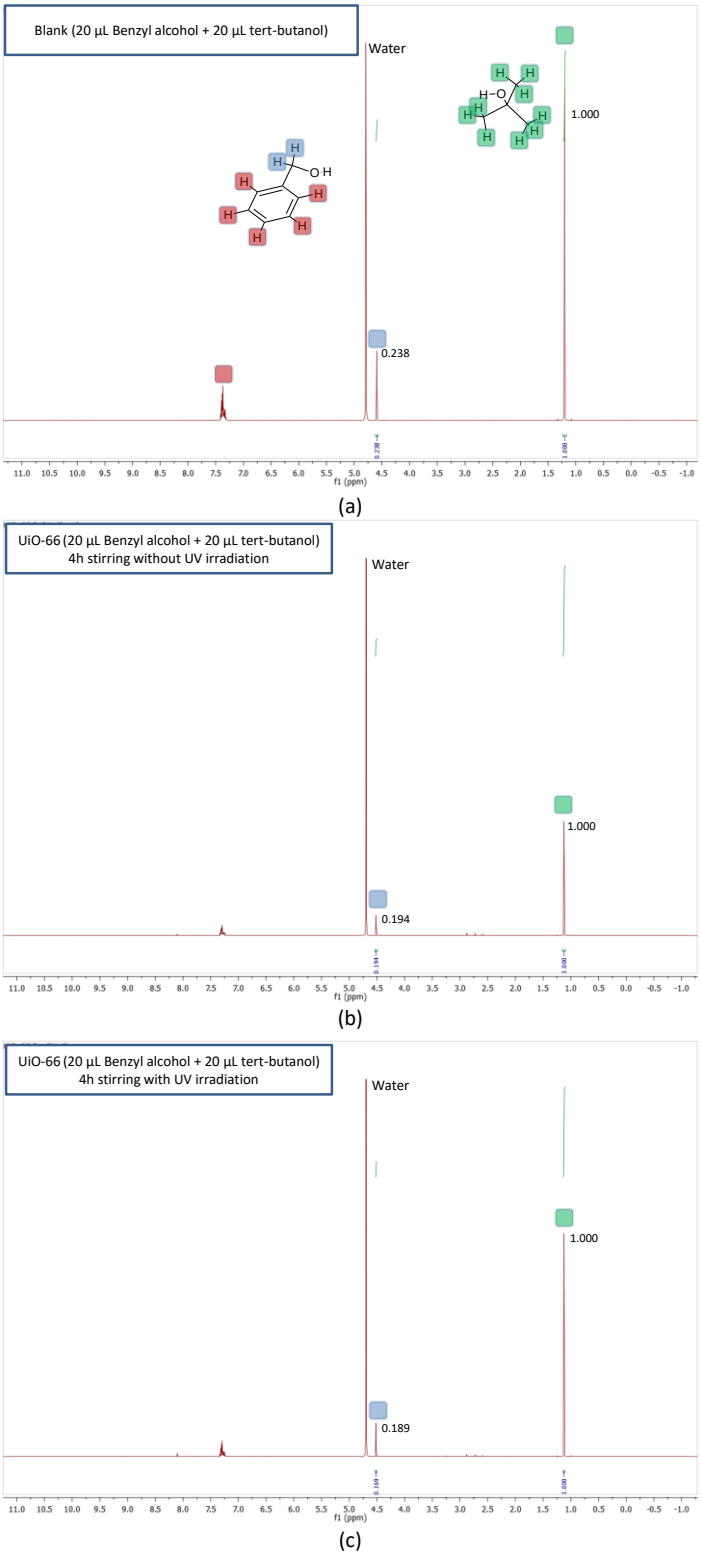

Fig. S22 (a) ^{1}H-NMR spectra of the blank solution, (b) the same blank solution after incorporating 50 mg of Zr_6/W_{12} and stirring for 4h, and (c) the same blank solution after incorporating 50 mg of UiO-66 and stirring for 4h while irradiating with a Hg lamp.

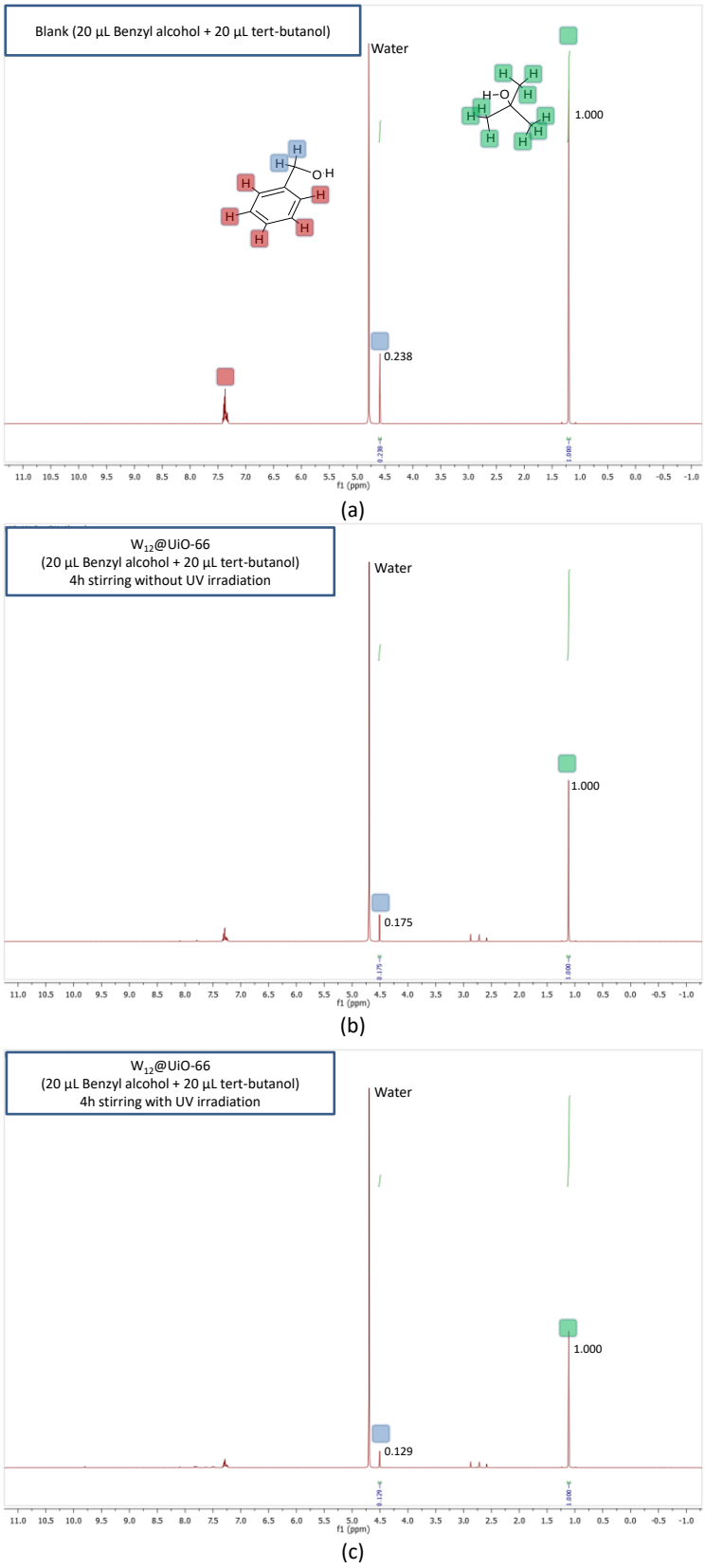

Fig. S23 (a) ^{1}H-NMR spectra of the blank solution, (b) the same blank solution after incorporating 50 mg of **W_{12}@UiO-66** and stirring for 4h, and (c) the same blank solution after incorporating 50 mg of W_{12}@UiO-66 and stirring for 4h while irradiating with a Hg lamp.

BENZYL ALCOHOL PHOTO-OXIDATION WITH SCAVENGERS FOR HYDROXYL AND SUPEROXIDE RADICALS·

The previous experiment was repeated adding isopropanol and hydroquinone to the reaction media as scavengers for hydroxyl and superoxide radicals, respectively.[12,13,14,15] The reaction product was analysed by 1H-NMR (Fig. S24).

[12] X. Zhao, Y. Zhang, P. Wen, G. Xu, D. Ma, P. Qiu, NH2-MIL-125(Ti)/TiO_2 composites as superior visible-light photocatalysts for selective oxidation of cyclohexane. *Mol. Catal.,* **2018**, *452*, 175-183.
[13] O. Fónagy, E. Szabó-Bárdos, O. Horváth, 1,4-Benzoquinone and 1,4-hydroquinone based determination of electron and superoxide radical formed in heterogeneous photocatalytic systems. *J. Photochem. Photobiol. A Chem.,* **2021**, *407*, 113057.
[14] Y. Zhang, N. Zhang, Z. R. Tang, Y. J. Xu, Graphene transforms wide band gap ZnS to a visible light photocatalyst. the new role of graphene as a macromolecular photosensitizer. *ACS Nano*, **2012**, *6*, 9777-9789.
[15] Y. Zhang, N. Zhang, Z. R. Tang, Y. J. Xu, Transforming CdS into an efficient visible light photocatalyst for selective oxidation of saturated primary C-H bonds under ambient conditions. **Chem. Sci., 2012**, *3*, 2812-2822.

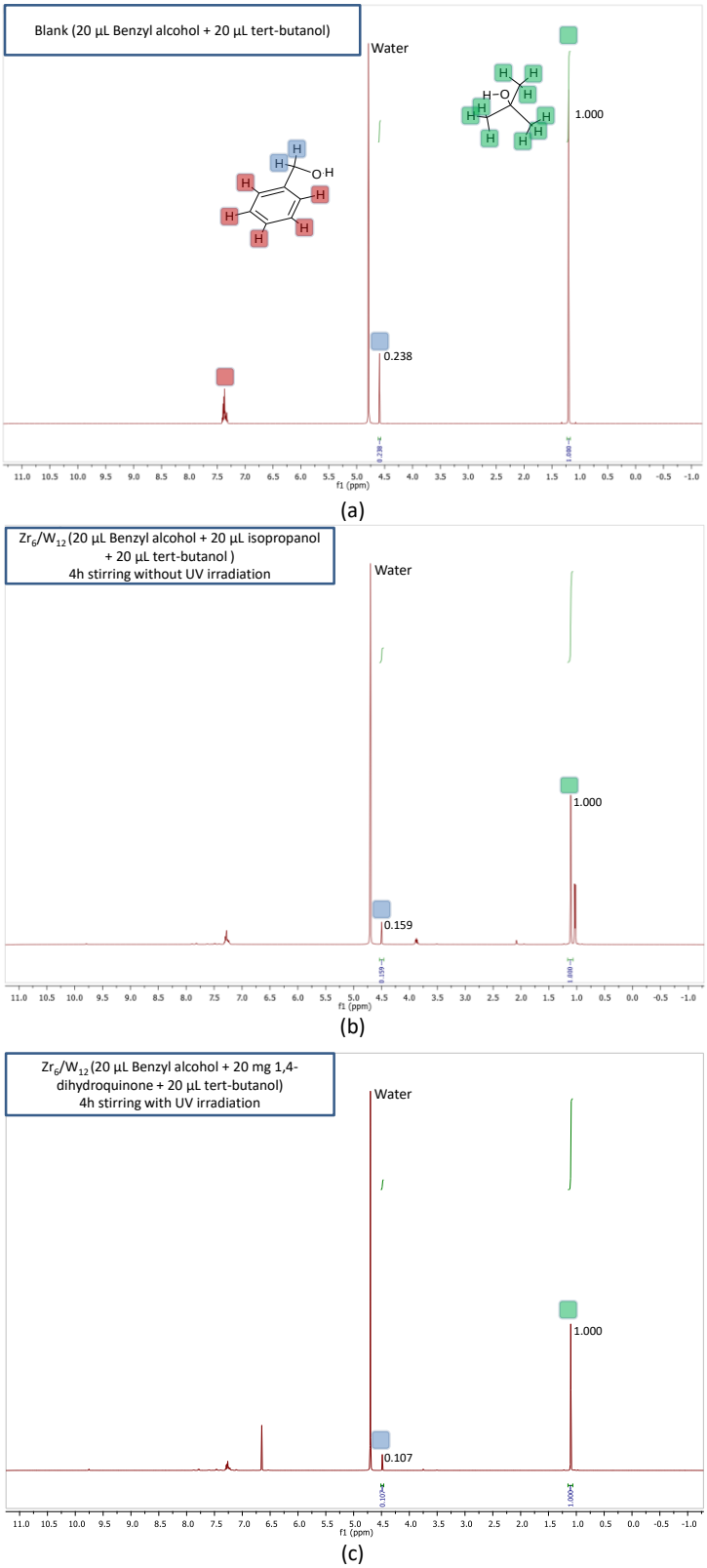

Fig. S24 (a) ^{1}H-NMR spectra of the blank solution, (b) the same blank solution after incorporating 50 mg of **Zr_6/W_{12}**, 20 µL of isopropanol (hydroxyl scavenger) and stirring for 4h while irradiating with a Hg lamp, and (c) the same blank solution after incorporating 50 mg of **Zr_6/W_{12}**, 20 mg of 1,4-dihydroquinone (superoxide scavenger) and stirring for 4h while irradiating with a Hg lamp.

S12. COMPUTATIONAL DETAILS

Density functional theory (DFT) calculations were performed with using Gaussian03,[16] using the hybrid Becke's three-parameter exchange functional in conjunction with the Lee-Yang-Parr correlation functional (B3LYP).[17] For both clusters, Los Alamos effective core potential combined with a DZ basis (LANL2DZ)[18] was chosen as basis set, since it provides a suitable compromise between accuracy and available computational power.[19] The structural models for each cluster were subtracted from the crystal structure of **Zr_6/W_{12}-MC**. As an approach of the electrostatic potential of each ion within the crystal, the charges were balanced by siting four monoions (F^- or Li^+ for $[Zr_6(\mu_3\text{-}O)_4(\mu_3\text{-}OH)_4(OOCC_6H_5OH)_8(H_2O)_8]^{4+}$ and $[SiW_{12}O_{40}]^{4-}$, respectively) around each cluster at distances of 6, 7 and 8 Å with respect the cluster centroid. The results are summarized in Fig. S25.

In all cases the highest occupied molecular orbitals (HOMO) are mainly comprised by the phenyl-π orbitals and μ-O-2p orbitals in the case of the Zr and W clusters, respectively. The lowest unoccupied molecular orbitals (LUMO), in both cases, are mainly built from the empty d-orbitals of the metals. Moving away the F^- anions from the $[Zr_6(\mu_3\text{-}O)_4(\mu_3\text{-}OH)_4(OOCC_6H_5OH)_8(H_2O)_8]^{4+}$ cluster centroid the energy of both HOMO and LUMO gets deeper, while greater distances for Li^+ respect the centroid of $[SiW_{12}O_{40}]^{4-}$ cluster, rises the energy levels. Note that the HOMO/LUMO energy differences are not meaningfully altered.

At this point, it must be considered that the shortest mean W···Zr_6(centroid) and Zr···W_{12}(centroid) (within the binodal 2D square supramolecular lattice (**sql**)) are

[16] Gaussian 03, Revision C.02, M. J. Frisch, G. W. Trucks, H. B. Schlegel, G. E. Scuseria, M. A. Robb, J. R. Cheeseman, J. A. Montgomery, Jr., T. Vreven, K. N. Kudin, J. C. Burant, J. M. Millam, S. S. Iyengar, J. Tomasi, V. Barone, B. Mennucci, M. Cossi, G. Scalmani, N. Rega, G. A. Petersson, H. Nakatsuji, M. Hada, M. Ehara, K. Toyota, R. Fukuda, J. Hasegawa, M. Ishida, T. Nakajima, Y. Honda, O. Kitao, H. Nakai, M. Klene, X. Li, J. E. Knox, H. P. Hratchian, J. B. Cross, V. Bakken, C. Adamo, J. Jaramillo, R. Gomperts, R. E. Stratmann, O. Yazyev, A. J. Austin, R. Cammi, C. Pomelli, J. W. Ochterski, P. Y. Ayala, K. Morokuma, G. A. Voth, P. Salvador, J. J. Dannenberg, V. G. Zakrzewski, S. Dapprich, A. D. Daniels, M. C. Strain, O. Farkas, D. K. Malick, A. D. Rabuck, K. Raghavachari, J. B. Foresman, J. V. Ortiz, Q. Cui, A. G. Baboul, S. Cliffor,, J. Cioslowski, B. B. Stefanov, G. Liu, A. Liashenko, P. Piskorz, I. Komaromi, R. L. Martin, D. J. Fox, T. Keith, M. A. Al-Laham, C. Y. Peng, A. Nanayakkara, M. Challacombe, P. M. W. Gill, B. Johnson, W. Chen, M. W. Wong, C. Gonzalez, and J. A. Pople, Gaussian, Inc., Wallingford CT, 2004.

[17] A. D. Becke, *J. Chem. Phys.*, 1993, **98**, 5648-5652; C. Lee, W. Yang, and R. G. Parr, *Phys. Rev. B*, 1988, **37**, 785–789.

[18] P. J. Hay, W. R. Wadt, *J. Chem. Phys*., 1985, **82**, 270.

[19] S. Reinoso, P. Vitoria, L. San Felices, L. Lezama, J. M. Gutiérrez-Zorrilla, *Chemistry - A European Journal*., 2005, **11**, 1538–1548.

7.95(0.19) Å and 8.49(0.21) Å, which suggests that a distance of 8 Å for the $Zr_6(\mu_3\text{-}O)_4(\mu_3\text{-}OH)_4(OOCC_6H_5OH)_8(H_2O)_8]^{4+}/F^-$ and $[SiW_{12}O_{40}]^{4-}/Li^+$ can be regarded as a good approach to model electrostatic potential of each ion within the crystal. Furthermore, it provides a relative disposition of HOMO/LUMO orbitals of $[Zr_6(\mu_3\text{-}O)_4(\mu_3\text{-}OH)_4(OOCC_6H_5OH)_8(H_2O)_8]^{4+}$ and $[SiW_{12}O_{40}]^{4-}$ clusters that fits to a Z-scheme photocatalytic system and it explains the experimentally observed synergy, since it makes feasible an efficient spatial separation of the charges by leaving the photogenerated e^-/h^+ in different molecular entities and hindering the undesired e^-/h^+ recombination.

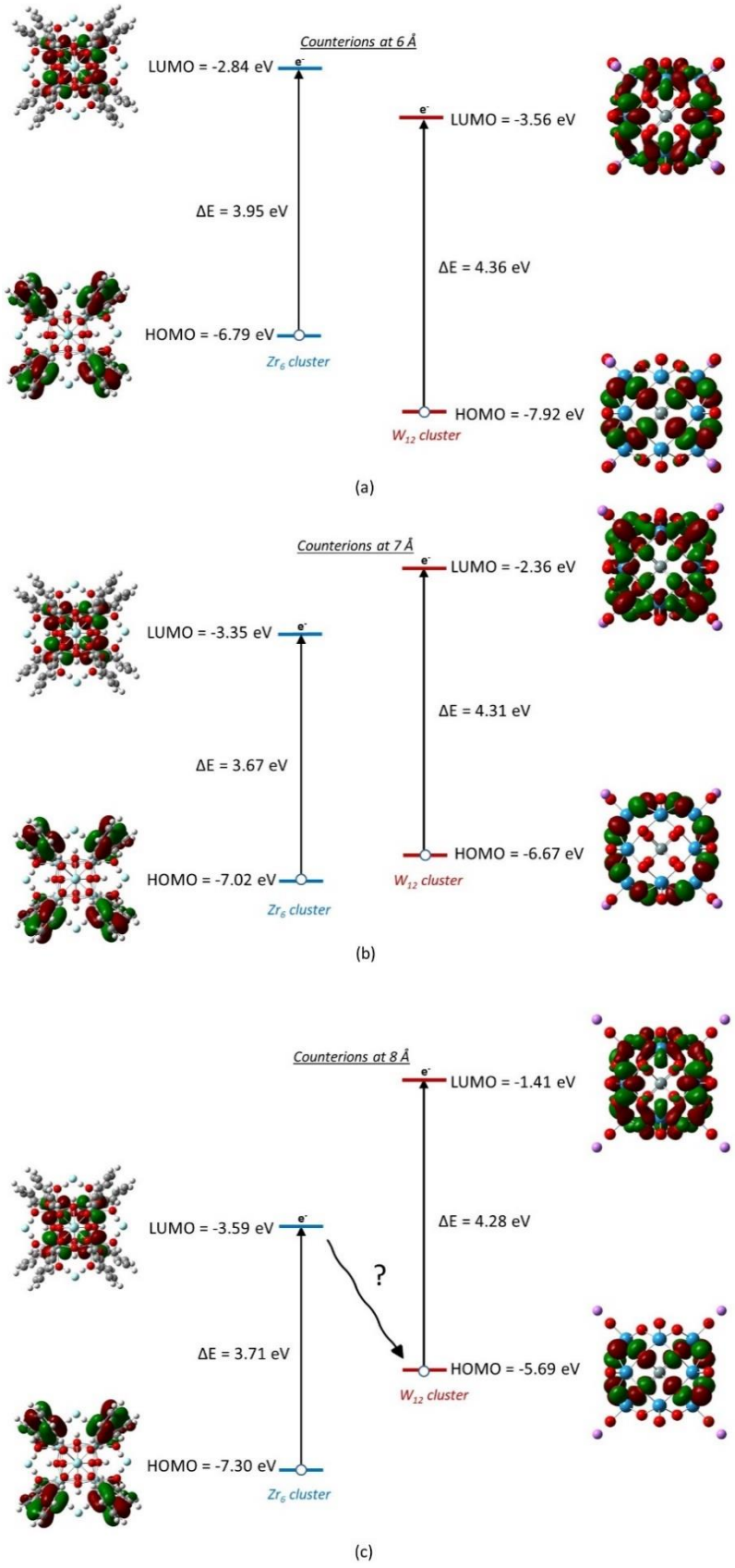

Fig. S25 HOMO and LUMO plots (isovalue = 0.05) and energies for each of the ionic cluster showing the influence of charge balancing counter-ions at different ion···cluster-centroid distances: (a) 6 Å, (b) 7 Å and (c) 8 Å. Blue and pink atoms represent F^- and Li^+ counterions, respectively.

S13. OPTICAL BAND GAP

The estimation of the band gap energy (E_g) was made from diffuse reflectance spectra measurements collected in a UV-2600 UV/Vis Shimadzu spectrometer. Spectra were measured at room temperature using $BaSO_4$ as reference material and converted to the Kubelka-Munk function[20] (Equation 1). In this equation the terms *K* and *S* express the absorption and dispersion of the sample, while R_∞ indicates the ratio between the reflectance of the sample and the reference material.

$$F(R_\infty) = \frac{K}{S} = \frac{(1-R_\infty)^2}{2R_\infty} \qquad \textbf{Eq. 1}$$

The converted spectra were employed to estimate the value of E_g by means of the modified Tauc expression (Equation 2),[21] in which $h\nu$ expresses the energy of the photon, α_o is a constant value and *n* takes the values of 0.5 and 2 for direct and indirect band transitions, respectively. Fig. S28 shows the converted spectra while Table S5 gathers the calculated E_g values for **Zr_6/W_{12}-MC**, **Zr_6/W_{12}-NP** and **CsW_{12}** assuming a direct band gap. The band bap for **UiO-66** was taken from the literature.

$$(F(R_\infty) \cdot h\nu)^{1/n} = \alpha_o(h\nu - E_g) \qquad \textbf{Eq. 2}$$

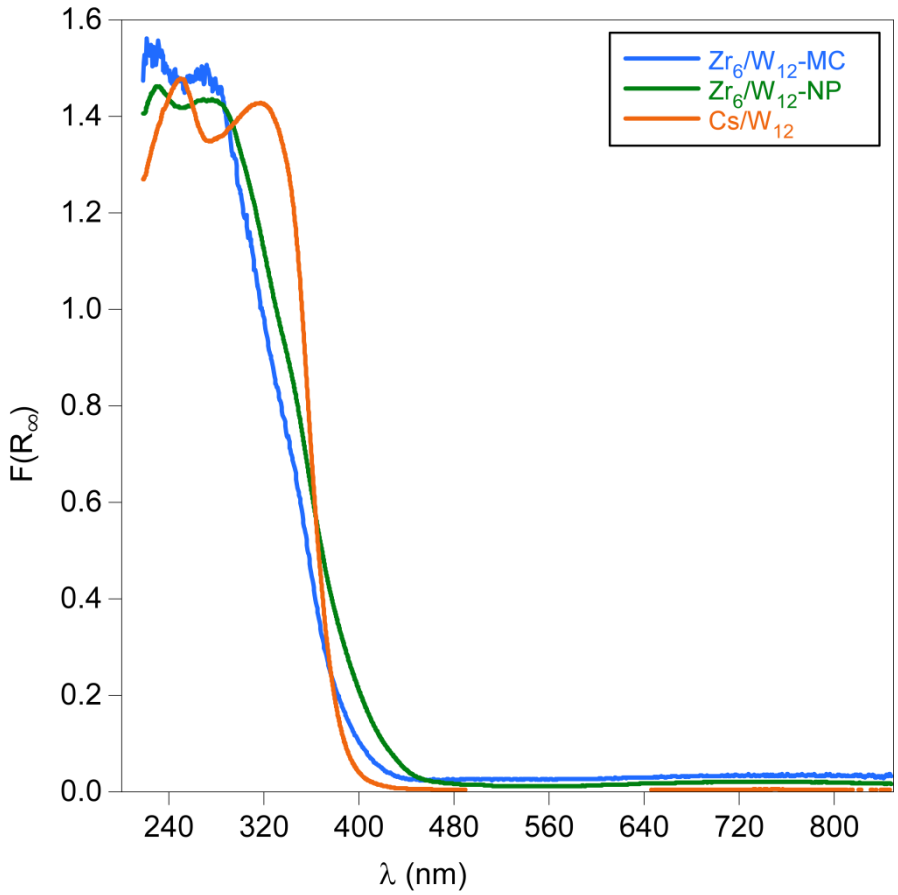

Fig. S26 Absorption UV/Vis spectra for **Zr_6/W_{12}-MC**, **Zr_6/W_{12}-NP** and **CsW_{12}**.

[20] P. Kubelka, and F. A. Munk, *Technol. Phys.*, 1931, **12**, 593-599.
[21] J. Tauc, R. Grigorovici and A. Vancu, *Phys. Status Solidi B*, 1966, **15**, 627-637; P. Makuła, M. Pacia and W. Macyk, *J. Phys. Chem. Lett.*, 2018, **9**, 6814–6817.

Table S5 Optical band gap energy values and coefficients of determination resulting from the spectra fitting to equation 2.

Compound	**E_g (eV)**	**R^2**
Zr_6/W_{12}-MC	3.54	0.9950
Zr_6/W_{12}-NP	3.42	0.9998
Cs/W_{12}	3.35	0.9964
UiO-66 [22]	3.20	

[22] E. Flage-Larsen, A. Røyset, J. H. Cavka and K. Thorshaug, *J. Phys. Chem. C*, 2013, **117**, 20610–20616.